New insights into the effects of porosity, pore length, pore shape and pore alignment on drug release from extrusion-based additive manufactured pharmaceuticals

Bin Zhang[a], Andy Gleadall[b], Peter Belton[c], Thomas Mcdonagh[a], Richard Bibb[d], and Sheng Qi[a] †

[a]School of Pharmacy, University of East Anglia, Norwich, UK

[b]School of Mechanical, Electrical and Manufacturing Engineering, Loughborough University, Loughborough, UK

[c]School of Chemistry, University of East Anglia, Norwich, UK

[d]School of Design & Creative Arts, Loughborough University, Loughborough, UK

† Corresponding author. E-mail: sheng.qi@uea.ac.uk

Abstract

Material extrusion-based additive manufacturing (ME-AM) has been recently adopted by the pharmaceutical field as a potential method for decentralised small-batch manufacturing of personalised solid dosage forms. The unique advantage of ME-AM is the ability to implement a wide range of micro-scale internal structures within a dosage form that can be used to manipulate the release kinetics of the drug. However, currently, there is no fundamental understanding of how the design of microstructures of a dosage form can control drug release. This study used polycaprolactone/ibuprofen as the model system to investigate four key geometric parameters of microstructures, printing pore length (by changing layer number), porosity (by varying the pore width), pore shape (by changing the filament intersection angles from 90° to 30°), and pore alignment, which allowed the construction of a wide range of interior microstructures within a drug-loaded 3D construct. This is the first work to have systematically investigated the interrelated effects of these parameters. The surface area/volume ratio (*SA/V*) of the constructs were simulated using the newly developed VOLume COnserving model (VOLCO). Four key points were found from this study: (1) drug release rate significantly increased with increasing porosity; (2) pore shape (or filament intersection angles) showed no significant effect on the drug release rate; (3) for the first time, a critical layer number (*Lc*) or (pore length) effect was observed and reported. The layer number only had a significant impact on drug release when below *Lc*; (4) when pore width was small, pore alignment significantly affected the release kinetics. The outcomes of this study provide clear principles and design guidance on using microstructures to control drug release from ME-AM solid dosage forms.

Keywords: Design for additive manufacturing, hot-melt extrusion, VOLCO model, geometrical parameters, microstructure control, controlled drug release.

Nomenclature

ME-AM	Material extrusion-based additive manufacturing
MDT	Mean dissolution time
PCL	Polycaprolactone
Ibu	Ibuprofen
VOLCO model	VOLume COnserving model
SA/V	Surface area/volume ratio
d_{xy}	Pore width
L	Pore length (height in the z axis defined by addition of layers)
Lc	Critical layer number or pore length
Q_E	Extrusion rate
T_g	Glass transition temperature
T_m	Melting temperature
V_{xy}	Printing speed
V_{exp}	Solid volume obtained from the experimental data
V_{VOLCO}	Solid volume obtained from the VOLume COnserving model
$\sigma_{filament}$	Index of printed filament deviation

1 Introduction

Additive Manufacturing (AM), also known as 3D printing, continues to attract increasing attention in the pharmaceutical science community due to its flexibility and customisability potential for personalised medicine manufacturing compared to traditional pharmaceutical manufacturing techniques [1, 2]. 3D printing allows the customised medicines [3, 4] and implants [5-7] to be tailored for individual patient's needs plays. In recent years, several 3D printing techniques have been applied in pharmaceutical research, such as stereolithography [8, 9], selective laser sintering [10], selective laser melting [11], inkjet printing [12, 13], and material extrusion based additive manufacturing (ME-AM) [14-17]. For thermally stable drugs, ME-AM is inexpensive in terms of hardware, operational costs and material wastage compared to other 3D printing techniques. One of its advantages is the flexibility of printing objects with various geometries with a wide range of materials [18-20] and has been widely reported for the proof-of-concept printing of polypills, implants, and other medical devices using drug-polymer mixtures [14, 21].

The use of microstructural design factors, such as surface area/volume ratio (*SA/V*), porosity and pore shape, to control drug release rates of ME-AM pharmaceuticals have been debated in the literature with inconsistent and sometimes contradicting results reported [15, 22, 23]. For example, Goyanes, Martinez et al. [16] used the fused deposition modelling (FDM) method to fabricate tablets with five inner geometries; cube, pyramid, cylinder, sphere and torus. The drug release results indicated that drug release from the tablets was not dependent on the surface area but instead on *SA/V*. Zhang et al. [24] produced tablets with variable outside shell thicknesses. They indicated that the shell structure acted as a barrier during the drug release study and a thicker shell led to slower drug release rate. Korte et al. [17] reported that the ME-AM tablets with denser infill led to a slower drug release; whereas Gültekin et al. [15] reported that the tablet infill had no effect on drug release rates, but increasing the tablet thickness decreased the drug release rates. In the literature, the most important geometric factor of ME-AM printed solid pharmaceuticals on drug release kinetics has been broadly agreed to be the overall *SA/V* ratio of the printed solid construct [16, 17]. However, in most cases, such effects were studied by changing either the overall outer shape or infill density.

In addition, in many of the studies the *SA/V* was calculated from the computer-aided design (CAD) file. However, it is known that noticeable discrepancies can exist between the final printed geometry and the original CAD file [25-27]. This led to a high degree of error in estimating key features of the prints such as *SA/V* using the CAD file [28, 29], and subsequently inaccurate results on the effects of *SA/V* on drug release rate. Thus, parallel comparisons of different studies in the literature on the effects of microstructure on drug release behaviour are difficult because samples were printed using different materials, sizes, shapes and geometries. Therefore, currently there is no clear systematic guidance supported by firm results on how to use internal microstructure to control drug release performance. This limits the further exploitation and industrial adoption of ME-AM for pharmaceutical manufacturing.

This study, for the first time, took a systematic approach to independently examining the effects of porosity, pore length, pore shape and pore alignment on drug release rate of 3D printed constructs. Each parameter was varied whilst keeping the other parameters constant in order to allow the fundamental effects of each structural parameter on drug release behaviour to be investigated. To evaluate the ME-AM printed constructs more accurately, the VOLume COnserving (VOLCO) model was employed for the *SA/V* calculation. The VOLCO model, developed by Gleadall *et al.* [29], is a computational method that simulates material extrusion during fabrication and generates a voxelised 3D-geometry-model of the predicted microstructure. The VOLCO model uses the experimental printing parameters and extrusion rate to simulate material deposition, including obstruction by previous extrusions to respect volume conservation; thus, the obtained *SA/V* of the simulated construct is a far more accurate estimation of the real print than the one obtained from the CAD design[29], which does not allow for volume conservation when extrusions overlap.

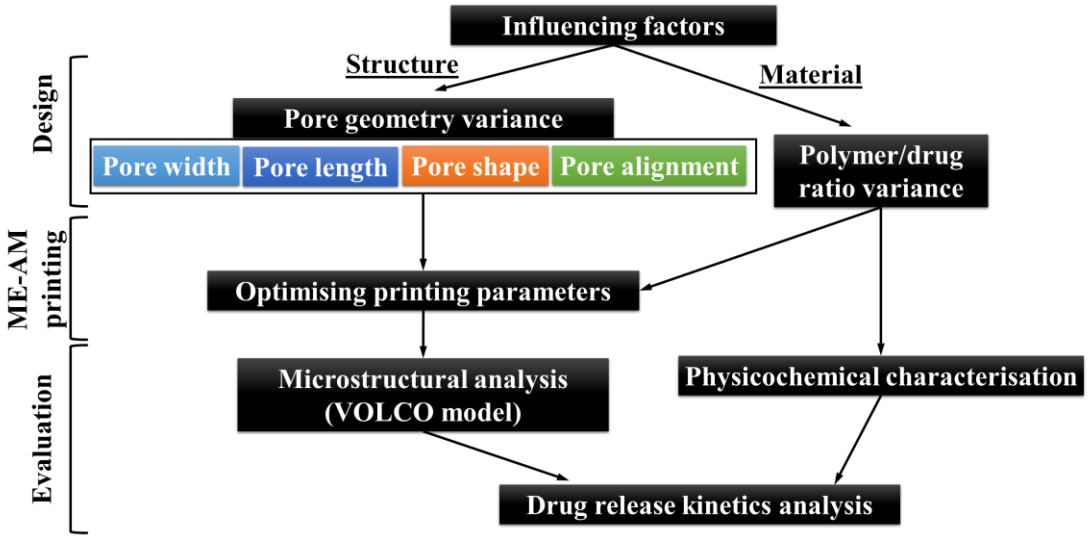

Figure 1. Flow chat of the experimental design and planning.

This study was carried out in three main stages: design, ME-AM printing and evaluation of the printed 3D constructs, as shown in **Figure 1**. **Design stage:** two influencing factors were investigated, which were pore geometry and polymer/drug ratio. Each parameter was varied whilst keeping the others constant. **ME-AM printing stage:** ME-AM process includes the hot-melt extrusion process and 3D printing process. The optimised processing parameters were obtained and used to produce all samples. **Evaluation stage:** the microstructures and the physicochemical properties of ME-AM printed 3D constructs were analysed prior to the drug release experiments. The microstructural and characterisation data were used to assist the interpenetration of the correlations among pore geometry, polymer/drug ratio and drug release kinetics.

2 Materials and methods

2.1 Materials

Polycaprolactone (PCL; average MW ~ 50,000 and density, ρ = 1.145 g/cm^3) was purchased from Perstorp (UK). Ibuprofen (tapped density, ρ_t = 0.48 g/cm^3) from BASF (Germany) was used as the model drug. Both PCL and ibuprofen were in powder form. All materials were used as received.

2.2 Designs of the 3D constructs

Four types of 3D constructs were designed for the examination of the geometry effect on the drug release. The detailed design parameters of the constructs are summarised

in **Table 1**. (1) 3D constructs with various porosity by varying the pore width from 0 - 2.1mm were designed; (2) lattice 3D constructs with various pore length (that is the height in the z axis defined by the addition of layers) by varying the layer number whilst the pore width was kept constant; (3) with the pore width and pore length kept constant, lattice 3D constructs with several intersection angles (90°, 60°, 30°) were designed to only change pore shape; (4) pore alignment achieved by offset building as staggered structures with the same pore width as the lattice structures.

Table 1. The CAD parameters of the different designs of the 3D constructs.

Sample name	**Tablet width (D_1) mm**	**Tablet length (D_2) mm**	**Tablet thickness (L) mm**
Pore width (highlighted in bold, 0-2.1 mm)*			
*PCL/5%Ibu_**0**_90°*	10	10	1.8
*PCL/5%Ibu_**0.4**_90°*	10	10	1.8
*PCL/5%Ibu_**0.6**_90°*	10	10	1.8
*PCL/5%Ibu_**1.2**_90°*	10	10	1.8
*PCL/5%Ibu_**2.1**_90°*	10	10	1.8
Pore shape (highlighted in bold, intersection angle 90°- 30°)*			
*PCL/5%Ibu_0.6_**90°***	10	10	1.8
*PCL/5%Ibu_0.6_**60°***	10	10	1.8
*PCL/5%Ibu_0.6_**30°***	10	10	1.8
Layer number (highlighted in bold, 2 - 18 layers with 0.6 &2.1 mm pore width)			
*PCL/5%Ibu_0.6_**2layer***	10	10	0.6
*PCL/5%Ibu_0.6_**4layer***	10	10	1
*PCL/5%Ibu_0.6_**8layer***	10	10	1.8
*PCL/5%Ibu_0.6_**10layer***	10	10	2.2
*PCL/5%Ibu_0.6_**12layer***	10	10	2.6
*PCL/5%Ibu_0.6_**18layer***	10	10	3.8
*PCL/5%Ibu_2.1_**2layer***	10	10	0.6
*PCL/5%Ibu_2.1_**4layer***	10	10	1
*PCL/5%Ibu_2.1_**8layer***	10	10	1.8
*PCL/5%Ibu_2.1_**10layer***	10	10	2.2
*PCL/5%Ibu_2.1_**12layer***	10	10	2.6
*PCL/5%Ibu_2.1_**18layer***	10	10	3.8
Layer configuration (highlighted in bold, stagger structure)**			
*PCL/5%Ibu_0.6_**stagger***	10	10	1.8

*PCL/5%Ibu_1.2_**stagger***	10	10	1.8
*PCL/5%Ibu_2.1_**stagger***	10	10	1.8
** The layer number is 8 for samples if it is not specified in the sample name.* *** with 8 layers, 0.6 , 1.2 & 2.1 mm pore width and intersection angle 90°*			

The first type was the cuboid layered lattice structures with a 90° intersection angle between extruded filaments. As shown in **Figure 2 (a)**, the 3D construct pore width in the *XY* plane is defined as d_{xy}which is the distance between two adjacent extruded filaments on the same layer. The extruded filament width (d) was designed to be the same as the 3D printing nozzle diameter (400 µm) used for printing. In order to obtain different porosities, pore widths (d_{xy}) of 0 µm, 400 µm, 600 µm, 1200 µm and 2100 µm were assigned. Porosity was defined as the fraction of unfilled volume to the total volume. The layer overlap (f) refers to the distance between the middle plane of two adjacent layers. Considering the practical condition of extrusion additive manufacturing, layer overlap (f) was fixed as 0.5 times the extruded filament diameter for all structures.

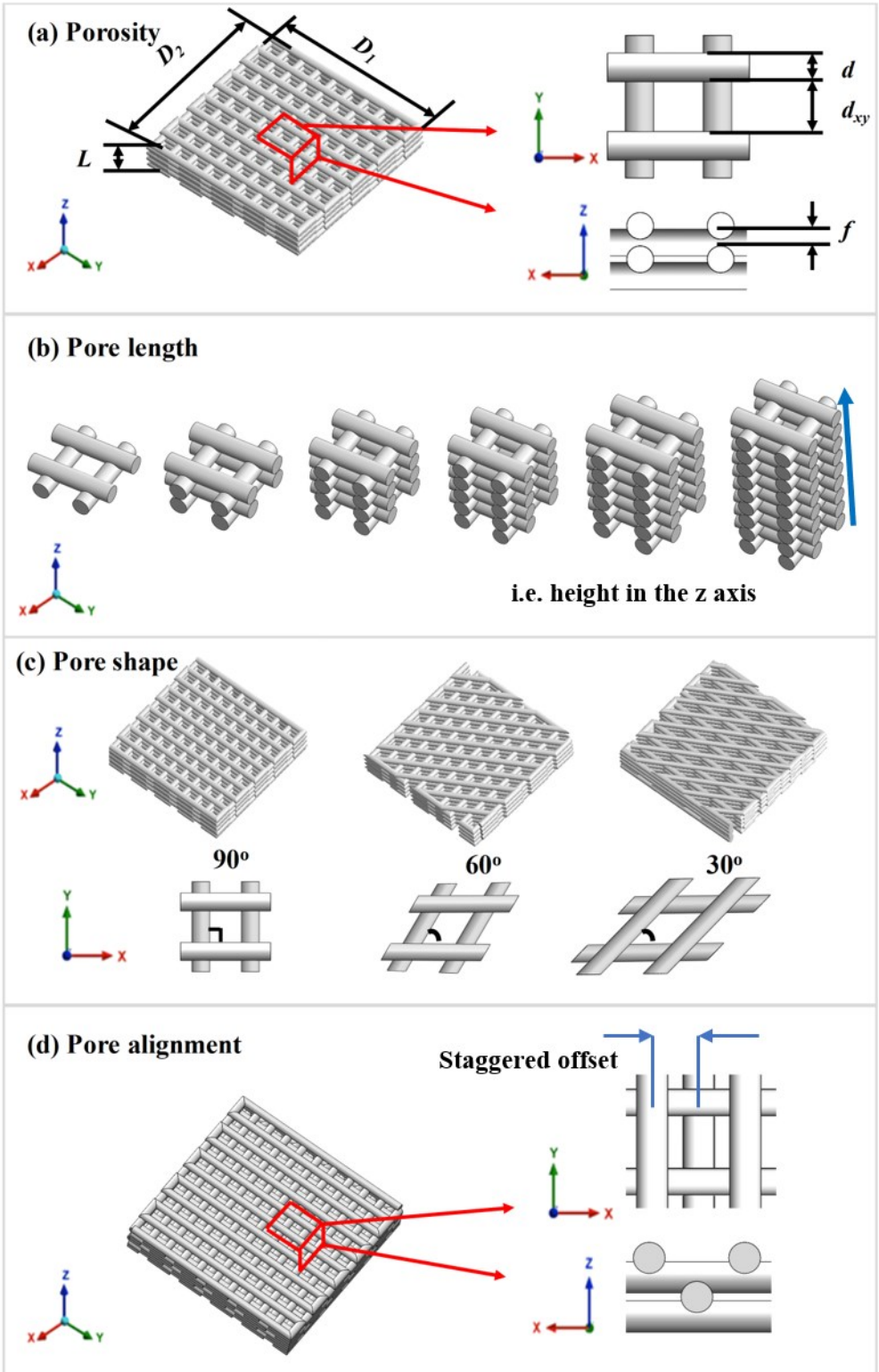

Figure 2. 3D "woodpile" structures with a lay-down angle of 90° with different porosity by (a) varying pore width (d_{xy}); (b) variable pore length of unit cells by changing the layer numbers of 2, 4, 8, 10, 12, 18; (c) 90°, 60°, 30° and associated unit cells in the *XY* plane, and (d) pore alignment was offset building as staggered structures.

The second type was the lattice 3D constructs with pore width and extruded filament width kept the same, while the pore length (*L*) was changed by varying the layer number from 2 to 18 layers. Pore length was defined as the formed thickness by increasing the overlapping layers, shown in **Figure 2 (b)**. The thickness is measured with respect to the *Z* direction. Pore length (*L*) of 0.6 mm, 1.0 mm, 1.8 mm, 2.2 mm, 2.6 mm, 3.8 mm were printed corresponding to 2-layers, 4-layers, 8-layers, 10-layers, 12-layers and 18-layers, respectively.

The third type of construct kept porosity, pore width, pore length (or layer number), and extruded filament width the same, while the extruded filament intersection angle was set at 90°, 60° and 30°. Pore shape was defined as the formed intersection angles by the two extruded filament orientations between adjacent layers, as viewed in the unit cells the *XY* plane shown in **Figure 2 (c)**; the angle is measured with respect to the *X*-direction.

The fourth type of 3D construct was designed by changing pore alignment to achieve a staggered structure, as shown in **Figure 2 (d)**. The extruded filament width, porosity, and pore length of the staggered structures were kept the same as the regular lattice.

2.3 3D constructs fabrication with ME-AM

2.3.1 Preparation of filaments by hot melt extrusion

Filaments were prepared from PCL and ibuprofen powders with a co-rotating twin screw Haake Minilab extruder (Thermo Fisher, Karlsruhe, Germany). 5% and 10% (w/w) ibuprofen concentrations were used as the low and high drug loading variants of the constructs. **Figure 3 (a)** describes the hot melt extrusion process for the filament manufacture. 5g of materials (i.e., PCL and ibuprofen powder) were accurately weighted then physically mixed via mortar and pestle for 5 min and fed into to the Haake Minilab extruder. The extrusion was performed at a screw speed of 100 rpm and a temperature of 80 °C, with 5-minute circulation time to ensure homogeneity of the mixing. The melted materials were extruded from a circular die with a screw speed in the range of 50 - 80 rpm onto a conveyer belt to obtain the filament diameter of 1.6 ± 0.5 mm. The filaments were measured using a digital calliper. The effects of any minor

variations in filament diameter were accounted for during analysis and simulation of constructs. The mechanical properties of the hot-melt extruded filaments were measured using a Texture analyser (Stable Micro Systems, Surrey, UK). The detailed methods and the results can be found in Supplementary Material, **Figure S1**.

2.3.2 ME-AM printing process

The 3D printer used in this study was a commercially available low-cost material extrusion 3D printer (Prusa i3 Mk3S, https://shop.prusa3d.com/en/). **Figure 3 (c)** describes the material extrusion process. The motion system comprises a print platform, which moves in the *Y* direction driven by stepper motors via belt drive, and a nozzle, which moves in *X* (also stepper motor and belt driven) and *Z* directions. The nozzle diameter was 400 µm, stepper motors drive the motion in the *Z* direction via twin lead screws with an overall resolution of 0.001 mm/step with a 1.8° step angle. During printing, the nozzle temperature was set at 100 °C and the print platform was not heated. The whole printing process was performed at room temperature (21 °C). The extruded-filament deposition is affected by the printing process parameters, i.e., printing speed (V_{xy}), and the extrusion rate (Q_E). V_{xy} was the nozzle movement velocity on the *XY* plane; Q_E is defined as the volume of material extruded per mm of nozzle travel. To optimise the 3D printing parameters, extrusion rates (Q_E) from 0.080 to 0.170 and printing speeds (V_{xy}) from 5.0 to 30.0 mm/s were investigated. G-codes were written using MATLAB 2019b (MathWorks, Natick, Massachusetts, United States) (**Figure 3 (b)**), which provided instructions to the printer that controlled the relative positions of the work stage and nozzle in all (*X, Y*, and *Z*) directions as well as the extrusion rate (Q_E) and printing speed (V_{xy}). A glass slide was used as a collecting substrate on the print platform. No support structures were used during the 3D printing of any of the constructs.

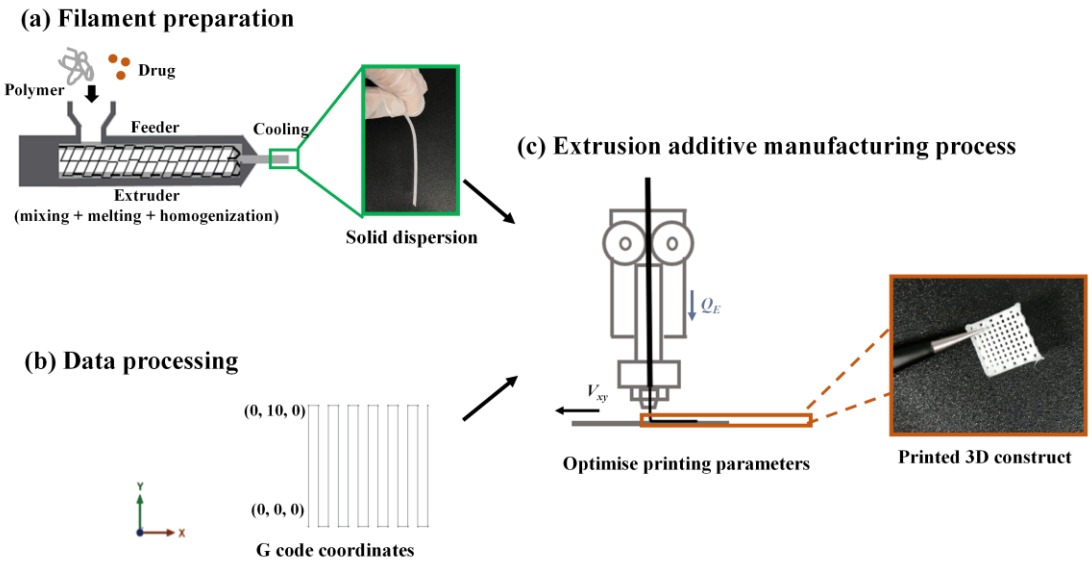

Figure 3. Schematic of the ME-AM printing a PCL/ibuprofen construct: (a) filament preparation - filaments were extruded from the hot-melt extruder; (b) data processing - G-codes were developed based on the predesigned CAD models; (c) extrusion based additive manufacturing process - the 3D construct was printed out after optimising the printing process parameters such as printing velocity (V_{xy}) and extrusion rate (Q_E).

2.4 Characterisation of 3D constructs

2.4.1 VOLCO model analysis

The VOLCO model, developed in a previous study [29], was used to simulate the material deposition based on the G-code files and the experimental weight of the printed constructs. This simulation was used to determine the total volume of deposited polymer for each construct, as described in section 2.4.2. The experimental weight data can be found in **Table S1** in the Supplementary Material. The standard deviations for three replicates of each construct type were used as an indicator to compared printing reproducibility of constructs with different microstructures. The solid volume (V_{solid}) and surface area (SA_{solid}) of 3D-geometry-models generated using VOLCO simulations were calculated in MATLAB and with MeshLab (ISTI – CNR, Pisa, Italy). The *SA/V* was calculated as the value of the solid surface area to solid volume using Equation (Eq) 1.

$$SA/V = \left(\frac{SA_{\text{solid}}}{V_{\text{solid}}}\right) \quad \textbf{Eq 1.}$$

2.4.2 Solid volume and porosity analysis

Experimental solid volume (V_{exp}) of the printed constructs was calculated based on their actual weight (M_{exp}) divided by their density (ρ_{exp}), as shown in Eq 2.

$$V_{exp} = \frac{M_{exp}}{\rho_{exp}} \quad \textbf{Eq 2.}$$

Considering the samples were printed with PCL mixed with ibuprofen, the density of ME-AM printed samples was calculated using Eq 3.

$$\rho_{exp} = \rho_1 * R_1 + \rho_2 * R_2 \quad \textbf{Eq 3.}$$

where ρ_1 and ρ_2 are PCL and ibuprofen density, which are 1.14 g/cm³ and 1.03 g/cm³, respectively [30, 31]. R_1 and R_2 are the weight fractions of PCL and ibuprofen within the printed samples. ρ_{exp} is the density of the printed constructs. The porosity was calculated from the percentage of the experimental solid volume (V_{exp}) of the total volume (V_{total}) of the printed construct using Eq. 4 and 5, where D_1, D_2, and L are the length, width, and thickness of the 3D constructs. They were measured by vernier calliper on the outer most edges.

$$V_{total} = D_1 * D_2 * L \quad \textbf{Eq 4.}$$

$$Porosity = (1 - \frac{V_{exp}}{V_{total}}) \quad \textbf{Eq 5.}$$

2.4.3 Shape fidelity and surface morphology analysis

A FDSC196 light microscope (Linkam Scientific, Surrey, UK) was used to inspect the printed constructs. The extruded filament width was quantified by measuring at least 50 filaments using Image J software (http://rsb.info.nih.gov/ij/); the data was exported for analysis, and statistical distributions were plotted using Origin software 2018 (OriginLab Corporation, Northampton, Massachusetts, United States). The results were presented as the mean ± standard deviation. The index of extruded filament deviation ($\sigma_{filament}$) was proposed to evaluate printing quality, which was defined as Eq. 6, where W_p is the extruded filament width, and d is the theoretical filament width (equal to the nozzle diameter). By varying the printing process parameters, the index of extruded filament deviation ($\sigma_{filament}$) was compared. For each set of the processing parameter, three filaments were produced and measured.

$$\sigma_{filament} = \frac{W_p - d}{d} \quad \textbf{Eq. 6}$$

The surface morphology of the printed samples was evaluated using scanning electron microscopy (SEM) with a Zeiss Gemini 300 (Carl Zeiss AG, Oberkochen, Germany). The samples were first sputter-coated with gold (10 nm). The images were taken at magnifications from ×25 to 500 with an acceleration voltage of 10 kV.

2.4.4 Physicochemical characterisation

The crystallinity of all the pristine materials, physical mixtures and 3D printed constructs were investigated by powder X-ray diffraction (PXRD) using a D5005 X-ray diffractometer (Siemens, Munich, Germany) with monochromatic CuKα radiation (wavelength =1.54056 Å). The samples were scanned from a 2θ angle of 15° to 60°, with a scan speed of 2°/min. The scan step was maintained at 0.02°, the resultant scan resolution was found to be 0.0025.

A Fourier transform infrared (FTIR) spectrophotometer (VERTEX 70, Bruker Optics, Ettlingen, Germany), equipped with a Golden Gate, Attenuated Total Reflectance (ATR) accessory (Specac Ltd., Orpington, United Kingdom) fitted with a diamond internal reflection element, was used to examine the raw materials and the prints. The spectra were collected over a wavenumber range of 500 - 4000 cm^{-1} with a resolution of 2 cm^{-1} at room temperature.

The thermal properties of raw polymers and printed parts were characterised using a Q1000 differential scanning calorimeter (DSC) (TA Instruments, Delaware, United States). TA Universal Analysis 2000 software was used for the data analysis on the duplicated samples, and the mean value was used to represent the results. DSC was performed to acquire the peak melting temperatures (T_m) of the raw polymer, ibuprofen and printed samples. The sample (3 - 5 mg) was accurately weighed in an Aluminium crimped DSC pan, and sealed using a lid with a pinhole. All samples were tested from 0 - 130 °C at a rate of 5°C/min. Nitrogen purge gas with a flow rate of 50 mL/min was used throughout the experiments. All tests on each type of construct were performed in triplicate.

2.5 *In vitro* drug release test

The *in vitro* drug release behaviours of the drug-loaded constructs were tested using a modified pharmaceutical dissolution test, in which the 3D printed constructs were placed in 25 mL of pH 7.4 phosphate-buffered saline (PBS) with agitated at 100 rpm at 37 °C in a KS 3000 control incubator shaker (IKA, Staufen, Germany). Sink condition was maintained during the drug release period. 3mL samples were extracted and replenished with an equal volume of fresh release medium at predesignated time intervals. The samples were placed in a 96-well quartz microplate for UV detection using a CLARIO star microplate reader (BMG Labtech, Ortenberg, Germany) at a wavelength of 266 nm (see Supplementary Material, **Figure S2**) [32]. The drug release experiments were performed in triplicate for each construct design. Numerical data were expressed as the mean ± standard deviation and analysed via Student's t-test to determine the differences among the groups. Statistical significance is indicated if p-values ≤ 0.05 represents as (*), ≤ 0.01 as (**), ≤ 0.001 as (***); while no significance if p-value > 0.05.

2.6 *In vitro* drug release data analysis

The mean dissolution time (MDT) (Eq. 7.) is a model-independent parameter that allows the direct comparison of drug release rates of dosage forms having different mechanisms controlling the drug release [33-35]. The value of MDT was employed to quantify drug release rate from 3D printed constructs with variable microstructures.

$$MDT = \frac{\sum_{j=1}^{n} t_{j^*}\,\Delta M_{j^*}}{\sum_{j=1}^{n} \Delta M_{j^*}} \qquad \text{Eq. 7.}$$

where j is the sample number, n is the number of dissolution sample times, t_{j^*} is the time at a midpoint between t_j and t_{j-1} and ΔM_{j^*} is the additional amount of drug dissolved between t_j and t_{j-1}.

3 Results

3.1 Optimisation of ME-AM processing parameters

The extrusion rate (Q_E) and printing speed in the *XY* plane (V_{xy}) directly influence extruded filament deposition. As shown in **Figure 4 (a)**, the extruded filament width was varied by changing the printing speed (V_{xy}) when the Q_E was 0.125 mm^3/s. When the V_{xy} was 5 mm/s, the extruded filament width was 446 ± 10.1 µm, which was wider

than the nozzle diameter (400 µm). Whereas, when the V_{xy} was 30 mm/s, the extruded filament was stretched, and the width of the deposited filament was 364 ± 2.3 µm, narrower than the nozzle diameter (400 µm). Once the V_{xy} increased to 150 mm/s, the deposition was interrupted, and the extruded filaments no longer showed a consistent diameter. The index of extruded filament deviation ($\sigma_{filament}$) was applied to evaluate the extruded filament width. If the $\sigma_{filament}$ value calculated using Eq. 6 is close to 0, it indicates that the extruded filament width is close to the nozzle diameter (400 µm). A comparison of the $\sigma_{filament}$ of PCL/ibuprofen under a range of the Q_E (0.080 - 0.170 mm^3/mm) and V_{xy} values (5 - 30 mm/s) is shown in **Figures 4 (b)**. The extruded filament width decreased with increasing the V_{xy} or reducing the Q_E. The printing parameters of V_{xy} of 20 mm/s and Q_E of 0.125 mm^3/mm provided the closest match of the extruded filament width to the nozzle diameter for the fabrication of PCL/ibuprofen extruded filament. These ME-AM parameters were subsequently applied for the fabrication of all of the 3D constructs with variable inner microstructures.

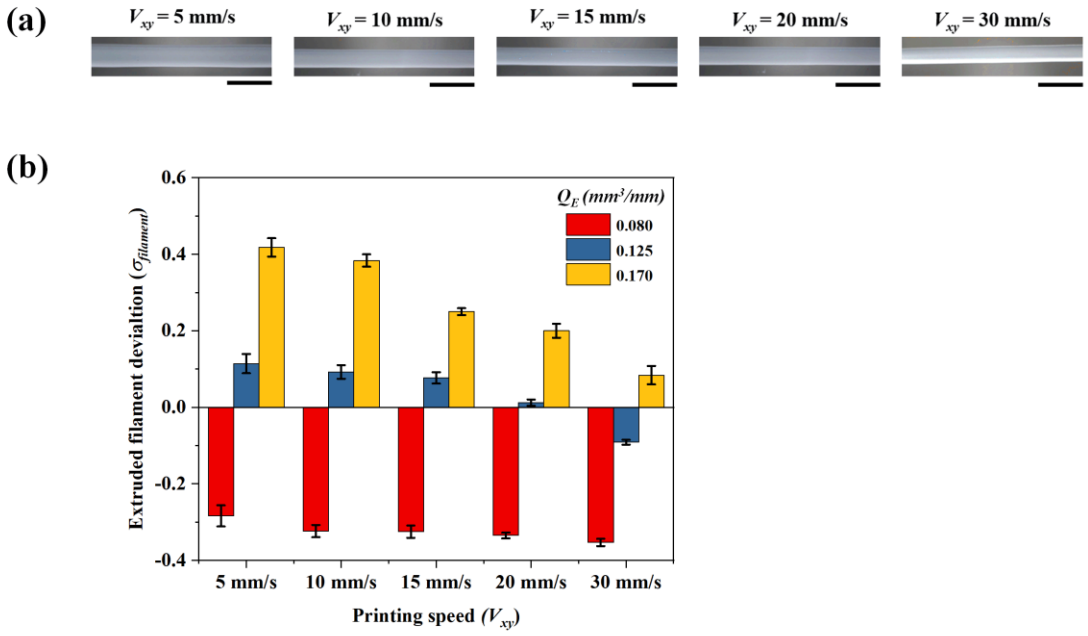

Figure 4. (a) PCL/ibuprofen extruded filament width changes with various printing speeds (V_{xy}) with extrusion rate (Q_E) 0.125 mm^3/mm, the scale bar is 900 µm; (b) extruded filament deviation ($\sigma_{filament}$) as an index to evaluate the extruded filament width under the designated printing speed (V_{xy}) and the extrusion rate (Q_E).

3.2 Microstructural analysis of 3D constructs

Experimental solid volume (V_{exp}) and porosity of the ME-AM printed 5% w/w ibuprofen loaded PCL/ibuprofen (PCL/5%Ibu) 3D constructs were calculated from Eq. 4 and 5 and summarised in **Table 2**. The results indicate that as pore width increases from 0 to 2.1 mm, V_{exp} the porosity of the construct decreases, as expected. However, changing the pore shape from 90°, 60° to 30° did not cause any significant difference in the V_{exp} or the porosity (P>0.05). The V_{exp} increased with increasing layer number in a logical manner. However, it is noted that there is a considerable difference between the porosity of the constructs with a low number of layers (2 - 4 layers) and higher layer numbers (8 - 18 layers). When changing the layer configuration, there is no significant difference in experimental volume (V_{exp}) or the porosity of the constructs with staggered and non-staggered structures.

Table 2. The solid volume and porosity measured experimentally, and the *SA/V* estimated from VOLCO model (V_{VOLCO}).

Sample name	Experimental volume (V_{exp}) (mm^3)	Experimentally measured porosity (%)	VOLCO volume (V_{VOLCO}) (mm^3)	VOLCO SA/V (mm^{-1})
The effects of pore width (0-2.1 mm)*				
PCL/5%Ibu_0_90°	235.5±32.0	0.2%±0.3%	235.5	1.8
PCL/5%Ibu_0.4_90°	135.2±3.8	27.3%±1.3%	134.1	7.3
PCL/5%Ibu_0.6_90°	111.7±2.6	39.6%±0.9%	111.7	8.4
PCL/5%Ibu_1.2_90°	85.3±5.5	54.4%±3.1%	84.6	8.6
PCL/5%Ibu_2.1_90°	55.9±2.3	66.2%±1.2%	55.9	9.8
The effects of pore shape (intersection angle 90°- 30°)*				
PCL/5%Ibu_0.6_90°	111.7±2.6	39.6%±0.9%	111.7	8.4
PCL/5%Ibu_0.6_60°	109.8±4.6	40.6%±2.7%	109.8	9.0
PCL/5%Ibu_0.6_30°	111.1±3.3	39.9%±1.1%	111.1	9.1
The effects of layer number (2 - 18 layers with 0.6 &2.1 mm pore width)				
PCL/5%Ibu_0.6_2layer	29.2±0.48	52.5%±4.5%	29.2	10.3
PCL/5%Ibu_0.6_4layer	78.3±1.9	43.2%±1.7%	78.4	5.6
PCL/5%Ibu_0.6_8layer	111.7±2.6	39.9%±1.2%	111.7	8.4
PCL/5%Ibu_0.6_10layer	152.0±1.6	36.7%±4.5%	152.0	7.7
PCL/5%Ibu_0.6_12layer	195.1±14.2	34.6%±4.1%	195.1	7.1
PCL/5%Ibu_0.6_18layer	253.4±19.3	36.9%±4.9%	253.4	8.5
PCL/5%Ibu_2.1_2layer	19.4±1.3	70.6%±1.7%	19.5	9.8
PCL/5%Ibu_2.1_4layer	34.7±2.6	73.9%±2.5%	34.7	9.0
PCL/5%Ibu_2.1_8layer	64.5±2.3	66.2%±1.2%	55.9	9.8
PCL/5%Ibu_2.1_10layer	97.3±5.7	59.4%±1.5%	97.3	7.3
PCL/5%Ibu_2.1_12layer	110.8±11.5	61.5%±4.0%	110.8	7.8
PCL/5%Ibu_2.1_18layer	175.2±9.4	56.1%±1.8%	175.2	7.3
The effects of layer configuration (stagger structure)**				
PCL/5%Ibu_0.6_stagger	128.7±3.9	39.7%±1.4%	128.7	7.4
PCL/5%Ibu_1.2_stagger	87.0±1.7	54.3%±0.9%	87.1	9.1
PCL/5%Ibu_2.1_stagger	72.2±2.8	65.0%±0.5%	70.2	9.0

**The layer number is 8 for samples if it is not specified in the sample name.*

*** with 8 layers, 0.6, 1.2 & 2.1 mm pore width and intersection angle 90°*

The VOLCO model was used to simulate the as-fabricated filament geometry and estimate the *SA/V* of the ME-AM printed 3D constructs. The voxel 3D-geometry-models exported from the VOLCO model are shown in **Figure 5**. The solid volumes of 3D constructs obtained from the VOLCO model (V_{VOLCO}) of all samples closely match the experimentally measured V_{exp}. This is because VOLCO allowed for the redistribution of material at obstruction points by conservation of volume. This is not the case for the original CAD model where entities can overlap in space; thus, VOLCO provides a more accurate estimation of the *SA/V* than CAD files (Supplementary Material **Table S2-5**) [32]. The influences of geometrical parameters (i.e., porosity, pore shape, pore length and pore alignment) on *SA/V* of the ME-AM printed construct estimated by VOLCO are summarised in **Table 2**. The results show pore width caused the most substantial change in *SA/V*. The *SA/V* of 3D constructs with pore width of 0 (i.e., 100% infilling density) was notably lower than others (pore width as 0.4 - 2.1 mm). When changing the pore shape (90°, 60° and 30°), the *SA/V* of 3D constructs with the same pore width (0.6 mm) showed little variation (being 8.4, 9.0 and 9.1, respectively). In terms of the effects of the pore length (or layer number), for both pore width of 0.6 mm and 2.1 mm, the *SA/V* of 3D constructs with 2 to 8 layers was higher than those with 10 to 18 layers. When the layer number increased above 10, there was no change in *SA/V*. Regarding the pore alignment, the *SA/V* of staggered structures decreased as the pore width decreased, which had a similar trend as those for lattice structures. When the same pore width (0.6 mm) was applied for lattice and staggered structures, similar experimental porosities (39.7% and 39.9%) were obtained and the *SA/V* had a slight variation (being 8.4 and 7.4, respectively).

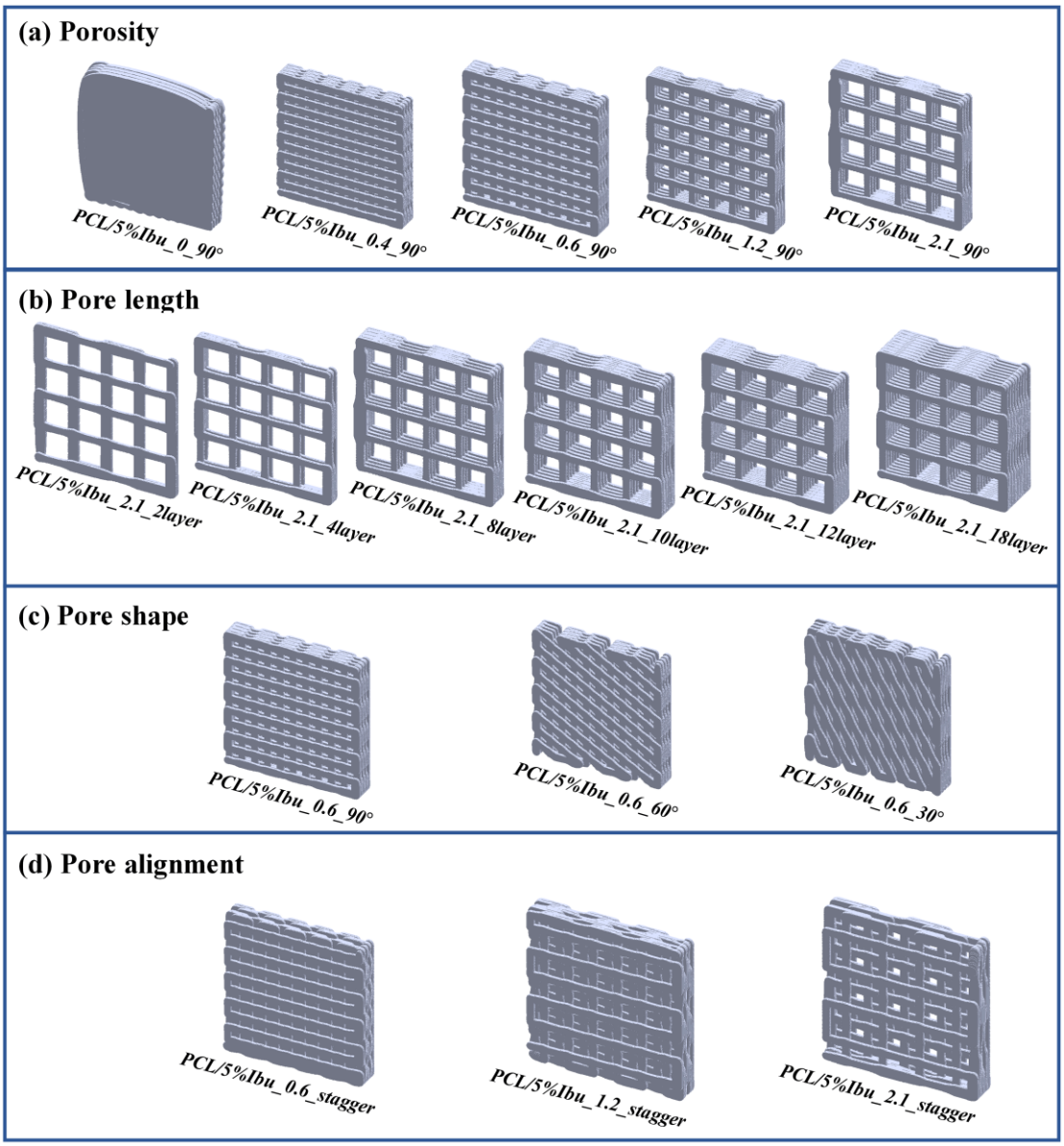

Figure 5. The 3D geometry models generated by VOLCO for samples with variable (a) porosity; (b) pore length; (c) pore shape; and (d) pore alignment.

3.3 Physicochemical characterisation of the drug-loaded 3D constructs

The SEM images of the ME-AM printed 3D constructs show rougher surfaces of the PCL/10%Ibu samples than the PCL/5%Ibu samples (**Figure 6**). It is noted that with increasing ibuprofen concentration from 0 to 10% w/w, the extruded filament width increased, and the corners of pores became more rounded. This increased extruded filament width with increasing drug loading may be due to the reduced thermoviscosity of the material during printing. Amorphous ibuprofen has a low glass transition temperature (T_g ≈ -50°C) and can substantially plasticise the amorphous portion of PCL

during printing [36]. The presence of melted ibuprofen in PCL disrupted the recrystallisation and solidification of PCL after deposition and led to wider spread of the material to give the wider extruded filament width.

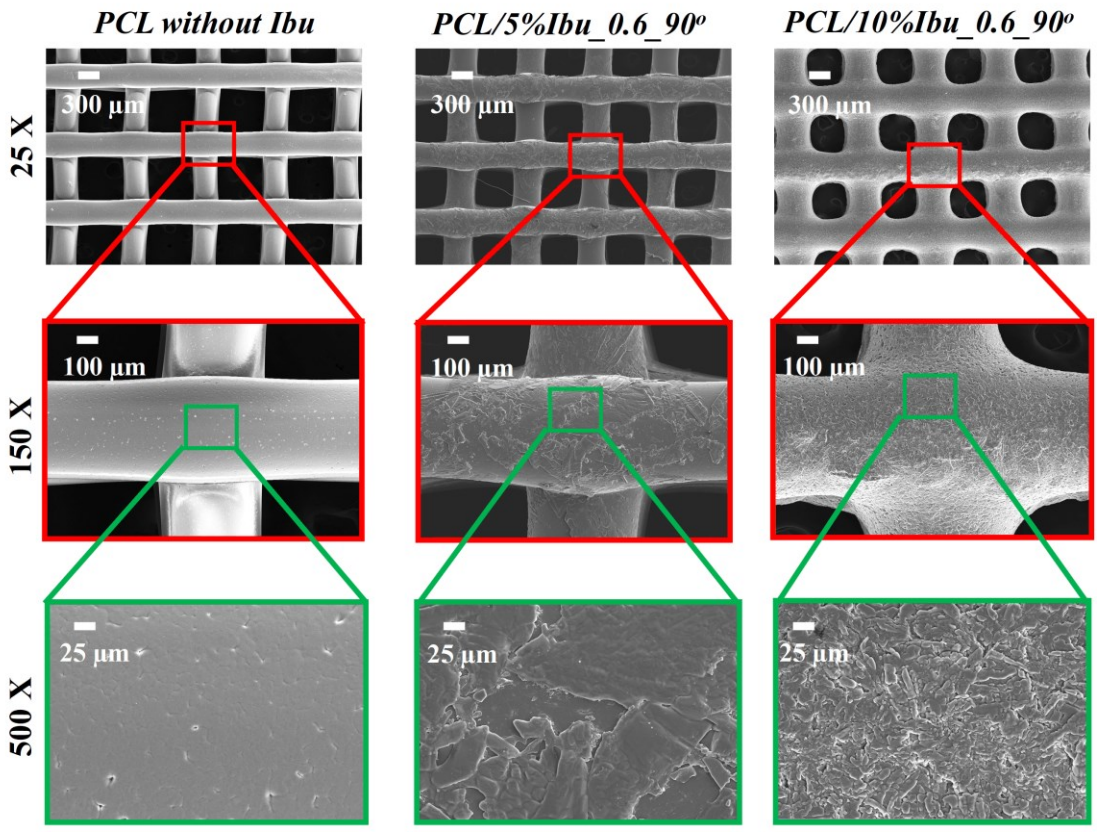

Figure 6. SEM images of *PCL without ibuprofen*, *PCL/5%Ibu_0.6_90°* and *PCL/10%Ibu_0.6_90°*.

The DSC results of PCL, ibuprofen, and the ME-AM printed PCL/Ibu samples are shown in **Figure 7 (a)**. The observed melting peaks (T_m) of pristine PCL and ibuprofen were 59.3 °C and 77.5 °C, respectively. The printed parts showed only peaks for the presence of PCL; 59.2 °C and 53.2 °C for the ME-AM printed sample of PCL/5%Ibu and PCL/10%Ibu, respectively. The lack of detectable melting of a crystalline phase for ibuprofen within the printed samples, and the depressed T_m of PCL indicated that the drug was mostly molecularly dispersed within the PCL polymer matrix. The depressed melting of PCL was caused by the incorporation of the drug which disrupted the molecular order and overall crystallinity of the PCL substance. The presence of a low quantity of crystalline ibuprofen is indicated by the PXRD data. As seen in **Figure 7 (b)**, the peaks at angles $2\theta = 21.4°$ and 23.8° correspond to the (110) and (200)

crystallographic planes of PCL polymer in both PCL/5%Ibu and PCL/10%Ibu [37]. With ibuprofen content increased from 5% w/w to 10% w/w, the intensity of the ibuprofen peak at 6.2° increased. This also agrees well with the SEM results and supports the observed surface roughness of the extruded filaments being related to the surface recrystallisation of ibuprofen. As shown in **Figure 7 (c)**, ATR-FTIR spectra of the ME-AM printed PCL/Ibu samples have no noticeable difference from the spectra of the physical mixtures of PCL and Ibu, indicating a lack of strong intermolecular interaction between PCL and ibuprofen.

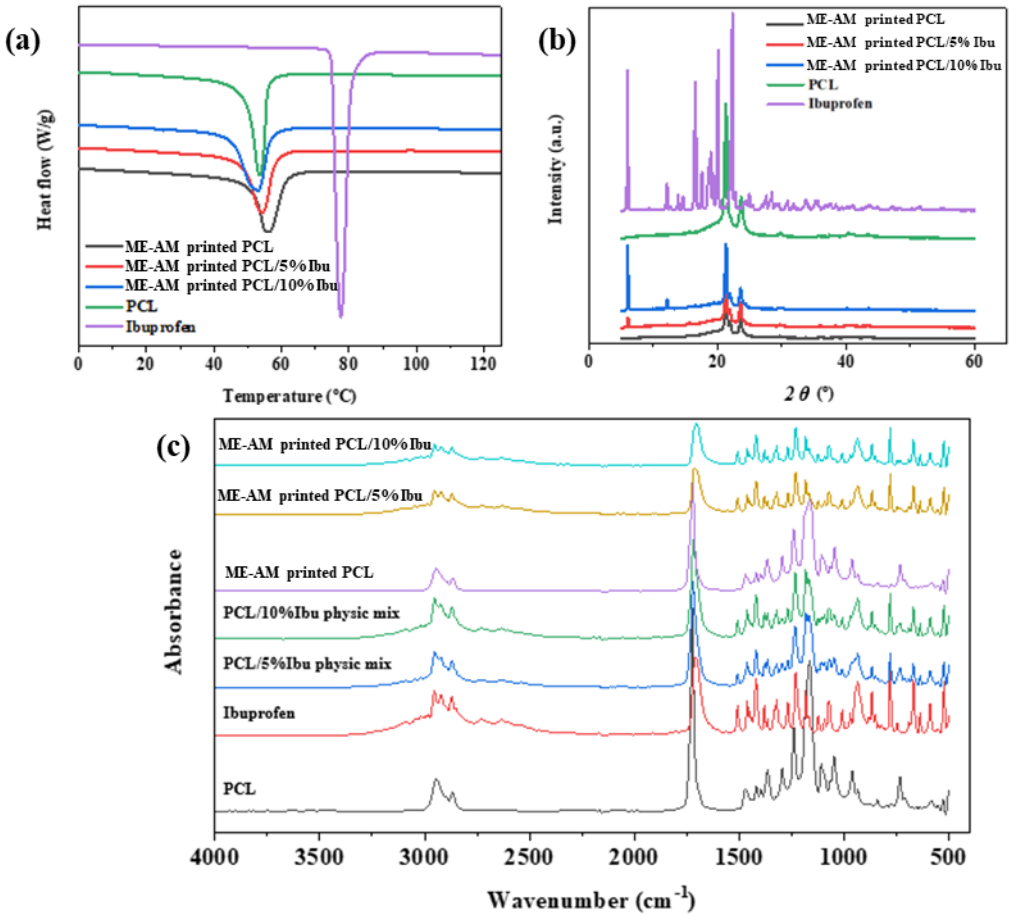

Figure 7. (a) DSC, (b) PXRD and (c) ATR-FTIR data of the ME-AM printed PCL, PCL/5%Ibu, PCL/10%Ibu, PCL and crystalline ibuprofen.

3.4 Effects of microstructure on *in vitro* drug release kinetics of ME-AM printed objects

3.4.1 The effects of drug loading

As seen in **Figure 8 (a)**, the crystalline ibuprofen (as the control) completely dissolved within 30 minutes, whereas the ME-AM printed drug-loaded constructs show much sustained ibuprofen release. The ME-AM printed PCL/Ibu samples containing high ibuprofen loading (10% w/w) had a faster release rate than the samples with 5% drug loading. Similar findings were reported in a study on ME-AM printed quinine loaded PCL by Kempin et al. [38]. As PCL is insoluble and non-swellable in the dissolution media, the diffusion of ibuprofen from the PCL-based extruded filament is the primary mechanism for controlling the drug release. The higher drug content would create a higher concentration gradient between the construct and the outer dissolution media compared to the construct with lower drug loading. This was further confirmed by MDT of *PCL/5%Ibu_0.6_90°*, which was significantly lower ($p<0.01$) than MDT of *PCL/10%Ibu_0.6_90°*, as shown in **Figure 8 (b)**.

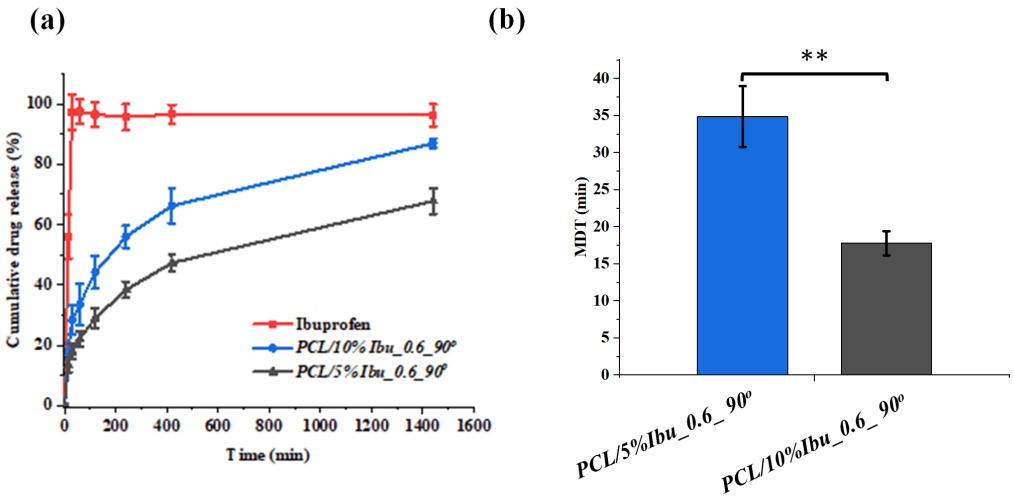

Figure 8. (a) The effect of drug loading on ibuprofen release profiles and (b) the MDT values of the ME-AM printed constructs with 5 and 10% drug loading in pH 7.4 PBS at 37 °C (n=3).

3.4.2 The effects of pore width

By keeping the overall dimensions and the pore shape constant, 0, 0.4, 0.6, 1.2 and 2.1 mm pore widths were used to investigate its effect on drug release rate (**Figure 9 (a)**).

As seen in **Figure 9 (b)**, the constructs with pore width of 2.1 mm, which had the highest porosity (circa 66.2%), showed more than 15.96% ± 1.59% of the drug was released within the first 15 minutes (**Figure 9 (b)**). In contrast, only 4.14% ± 1.27% of the drug was released in the first 15 minutes from the samples with 0% porosity. The drug release rate increased with increasing pore width. As seen in **Figure 9 (c)**, the MDT data also confirms that there was a significant difference among the samples as pore width changed from 0 to 2.1 mm. This can be attributed to the increase in SA/V simulated using the VOLCO model (**Table 2**). The MDT of the sample with no pores was significantly higher ($p<0.001$) than other groups because the drug needed to diffuse through multiple extruded filaments, rather than to the surface of a single extruded filament.

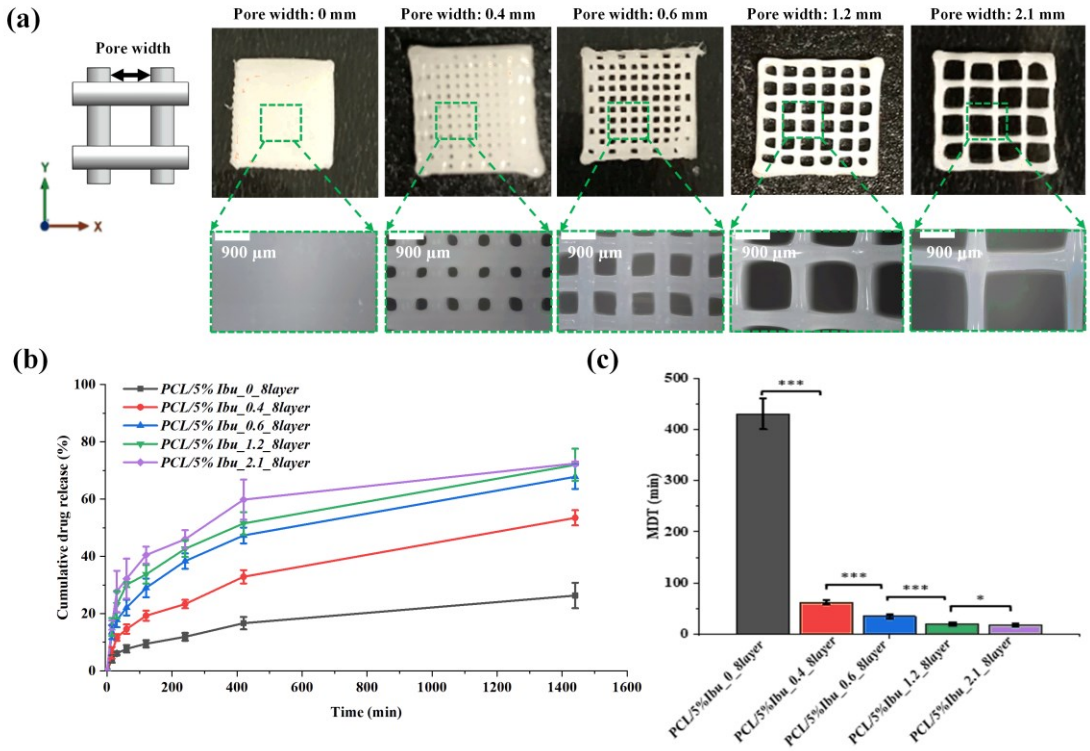

Figure 9. (a) The appearances of the ME-AM printed 3D constructs with variable pore width, (b) the effect of pore width on ibuprofen release profiles and (c) the MDT values of PCL/*5%Ibu_0_90°*, *PCL/5%Ibu_0.4_90°*, *PCL/5%Ibu_0.6_90°*, *PCL/5%Ibu_1.2_90°* and *PCL/5%Ibu_2.1_90°* in pH 7.4 PBS at 37 °C (n=3).

3.4.3 The effects of pore length

With a fixed pore shape of 90° and pore width of 0.6 or 2.1 mm, the effect of the number of layers within a 3D construct on the drug release was investigated. As seen in **Figure 10**, the drug release rate decreased with increasing numbers of layers for the range 2 to 10 layers. This was true in both cases of pore width (0.6 and 2.1 mm). In both groups, when further increasing the number of layers above 10, the drug release rates no longer changed (**Figure 10a and 10b**). The significant differences in the MDT values of the constructs with 2, 4, 8 and 10 layers for both pore width 0.6 mm and 2.1 mm is summarised in **Figure 10 (c)**. This is a highly noteworthy finding. The practical implication of this finding is that if one wants to use the pore width to control the drug release rate, the critical minimal number of layers should be first determined. For the model system of ibuprofen and PCL with an extruded filament width of approximately 0.4 mm used in this study, the critical minimal layer number is 10 layers. When 10 or fewer layers are used within a construct, the drug release rate is not only affected by the pore width, but also the number of layers (Supplementary Material, **Figure S3**) [32].

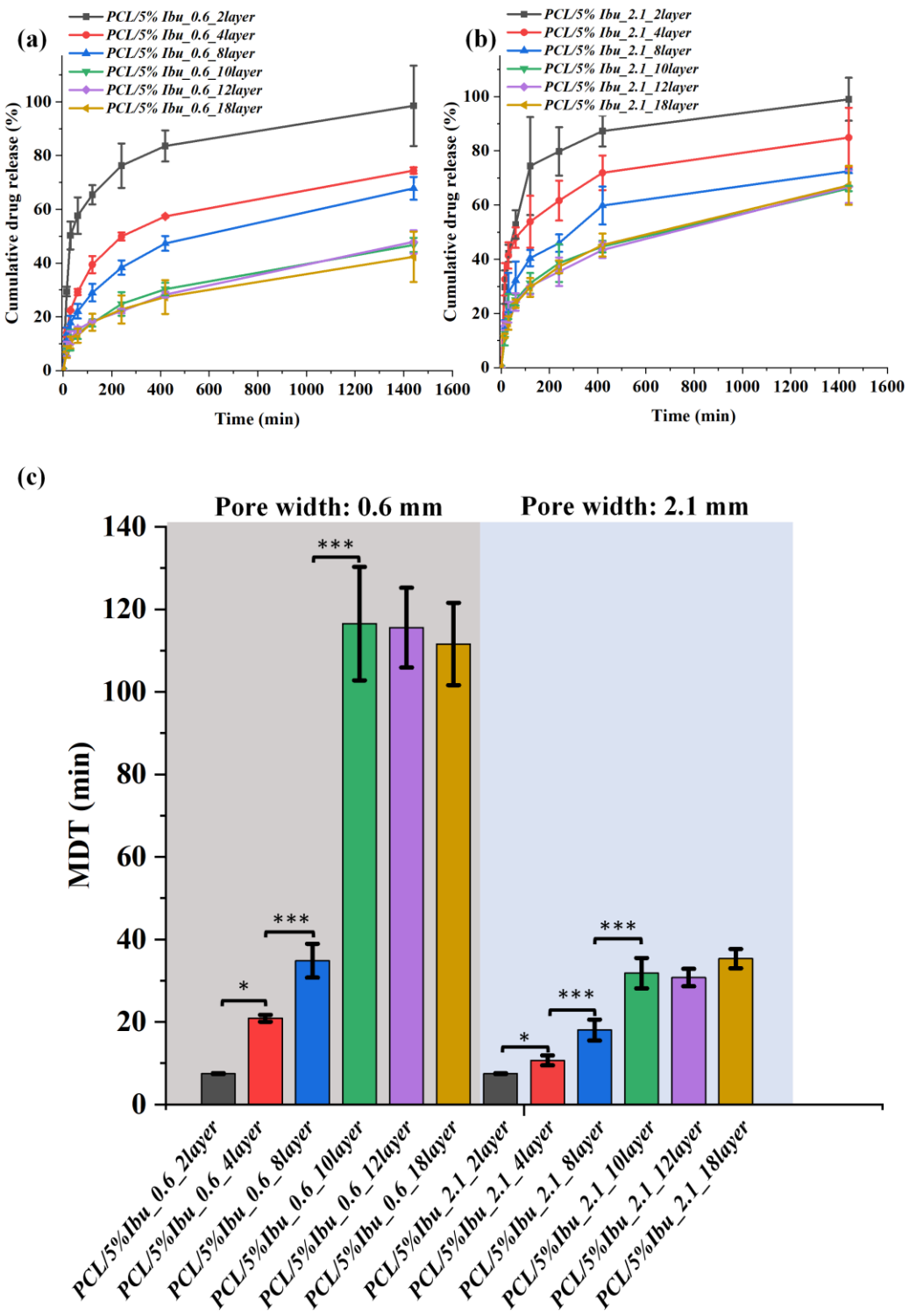

Figure 10. The effect of pore length (or layer numbers) on ibuprofen release profiles with pore width of (a) 0.6 mm and (b) 2.1 mm, and (c) the MDT values of the printed samples with 2 to 18 layers in pH 7.4 PBS at 37 °C (n=3).

3.4.4 The effects of pore shape

Pore shape is a geometrical parameter that has not been widely investigated in the literature in terms of its effect on the drug release of 3D printed pharmaceutical solids. In this study, by simply changing the extruded filament intersection angle, constructs with three different pore shapes were produced (**Figure 11 (a)).** All had a similar porosity of circa 40.0% ± 0.5%, and were used to investigate the effects of pore shape on drug release. As seen in **Figure 11 (b)**, there is no significant difference (P>0.05) in the release rates for different pore shapes, indicating that pore shape had much less influence on the drug release profile than porosity and pore length.

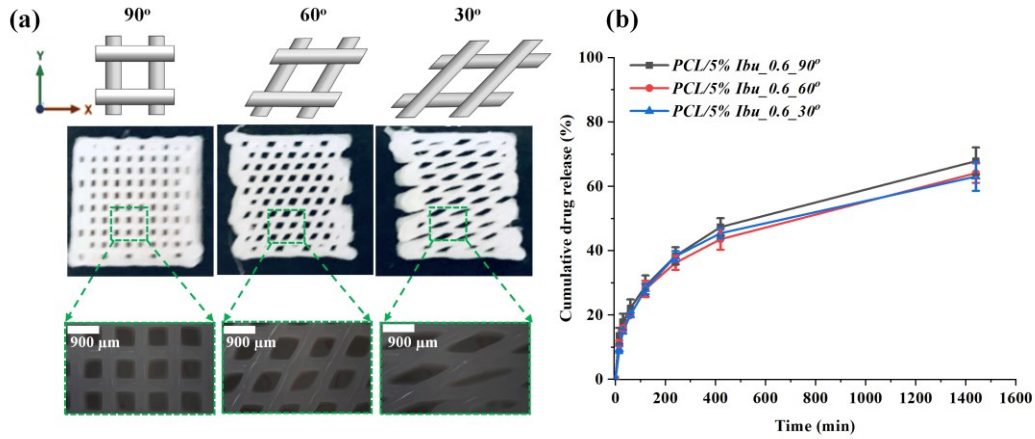

Figure 11. (a) The appearances of the ME-AM printed 3D constructs with variable pore shape, (b) the effect of pore shape on ibuprofen release profiles from extrusion based additive manufactured *PCL/5%Ibu_0.6_90°*, *PCL/5%Ibu_0.6_60°*, *PCL/5%Ibu_0.6_30°* in pH 7.4 PBS at 37 °C (n=3).

3.4.5 The effects of pore alignment: aligned vs staggered

The effect of pore alignment on drug release rate has not been investigated in the literature but is known to be of critical importance for other dynamic procedures such as cell seeding [39]. Structures with pores aligned (i.e., lattice structures) or staggered (offset by 50% of the pore unit cell) on each 3D printed layer were evaluated to identify the effect of pore alignment on drug release rates. Both aligned and staggered constructs had constant pore width, pore length, overall porosity and *SA/V*. **Figure 12 (a)** shows the design of the staggered layer configuration with pore widths of 0.6, 1.2 and 2.1 mm. Similar to the trend observed in the constructs with aligned pores, in the constructs with lattice structures (section 3.4.2) the drug release rate of the staggered 3D construct

increased as pore width increased from 0.6 to 2.1 mm (**Figure 12 (b)**). However, despite the similar pore width/porosity/*SA/V* ratio of staggered and aligned-pore structures, the drug release rates of the constructs with a staggered structure were significantly slower than the ones with aligned lattice structures. This can only be attributed to the layer offset arrangement in the staggered structures. However, the difference decreased as pore width increased, and no statistically significant difference ($P>0.05$) is seen in the release rates of the constructs with staggered and aligned pores for a 2.1 mm pore width (**Figure 12 (b)**). This suggests that as pore width reduced, the effect of staggered alignment between layers on media flow/ingress through the construct and subsequently the drug release became magnified (Supplementary Material, **Figure S4**) [32]. This is to be expected since the staggered structure with a 2.1 mm pore width had uninterrupted pores through the construct with an approximate width of 0.85 mm, potentially impeding flow/ingress no more than a construct with aligned pores of width 0.85 mm.

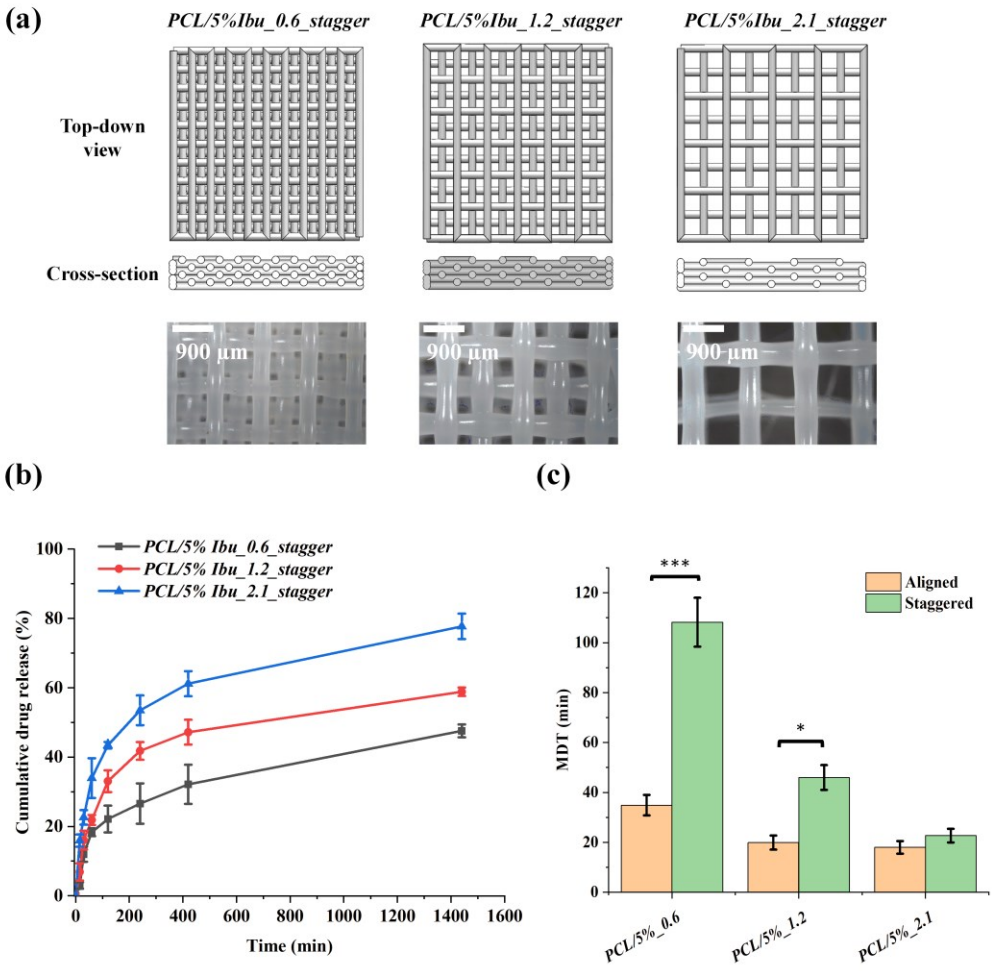

Figure 12. (a) The CAD model and the appearances of ME-AM printed staggered constructs with variable pore width, (b) the effects of pore width on ibuprofen release profiles from staggered structure and (c) the comparison of the MDT values of the constructs with staggered and aligned designs in pH 7.4 PBS at 37 °C (n=3).

3.5 A case study using microstructures to tailor drug release rate

Here we present a case study to demonstrate how our findings from the effect of pore alignment can be used to tailor drug release rate when porosity and pore volume are kept constant. A new 3D design combining staggered pores (central region) and aligned pores (perimeter regions) is shown in **Figure 13 (a)** along with specimens with all aligned or all staggered pores. The design can be seen in more detail in the supplementary material Video S1 [32]. The experimental porosities were similar for all

three constructs (39.6%±0.4%), as were *SA/V* ratios simulated by VOLCO (all *SA/V* ratios were 8.0 ± 0.6 mm^{-1}) (see Supplementary Material, **Figure S5**) [32]. As seen in **Figure 13 (b)**, the manipulation of pore alignment led to different drug release rates, with the staggered structure being slowest, the aligned structure being fastest, and the new design of mixed staggered and aligned pores having an intermediate drug release rate. **Figure 13 (c)** confirms the significant differences ($P<0.05$) in the MDT values among the three constructs. The results of this case study demonstrated translatability of the results in this study (Section 3.4.5) and showed how they can be used to inform the structural design of constructs to tailor drug release rate. Depending on the design requirement for a specific application, it is possible to control drug release rate whilst keeping other parameters constant such as pore size or porosity and crucially with no change to the feedstock materials or 3D printing equipment. This demonstrates the ability to customise or personalise drug release rates purely through geometric design offering enormous potential for distributed manufacture, on site, on demand with a single machine and single standard feedstock.

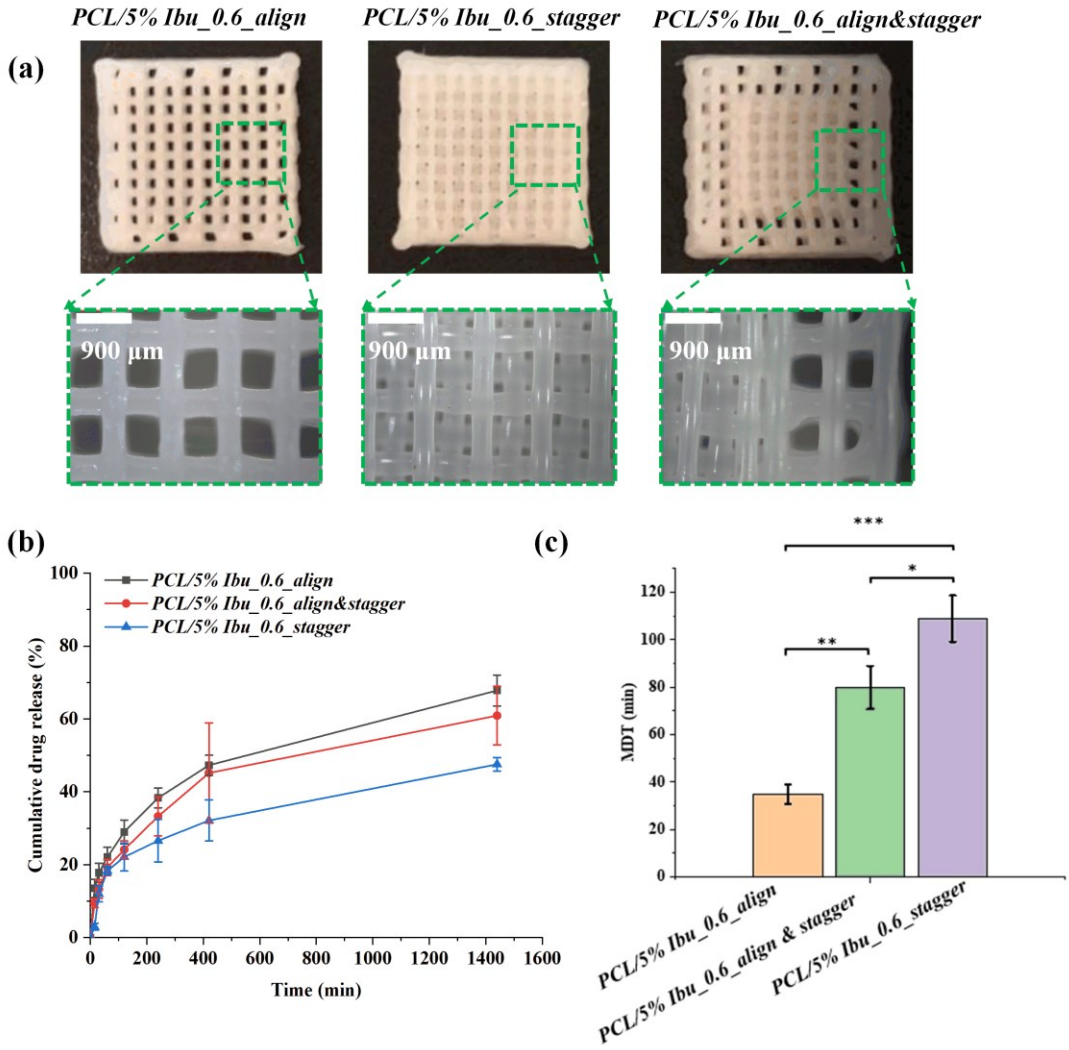

Figure 13. (a) The appearances of the ME-AM printed constructs with constant porosity and print settings, but minor adjustments to the print path to combine aligned pores (perimeter regions) and staggered pores (central region) led to tailored drug release, (b) the drug release profiles and (c) the MDT values of the constructs with aligned, staggered and a combination of both in pH 7.4 PBS at 37 °C (n=3).

4 Discussion

4.1 The correlations between pore geometries and drug release kinetics

A clear understanding of the correlations between pore geometries and drug release kinetics can provide guidance on how to effectively use the pore design to control drug release. The *SA/V* values (**Table 2**) of all the 3D constructs were plotted against their measured MDT values to examine any direct correlations between *SA/V* and drug release rate (see Supplementary Material **Figure S6**). The results confirmed that the

lowest *SA/V* leading to the highest MDT (*PCL/5%Ibu_0_8layer*), and the highest *SA/V* leading to the lowest MDT (*PCL/5%Ibu_2.1_2layer*). However, no consistent trend of correlation between *SA/V* and MDT was observed. For example, *PCL/5%Ibu_0.6_18layer* had a similar *SA/V* (circa 8.4) as the constructs with *PCL/5%Ibu_0.6_8layer*, but the MDT value of *PCL/5%Ibu_0.6_18layer* (111.6±9.9) is significantly higher than the MDT value of *PCL/5%Ibu_0.6_8layer* (34.9±4.1). In order to unravel any potential correlations or interactions between the pore geometries and drug release kinetics, the MDT and all parameters associated with the pore geometries (i.e., porosity, pore length, pore shape and pore alignment) were individually plotted and analysed. The MDT values were used as the quantification of the drug release rate (being the *Y*-axis) and the higher MDT indicate the slower drug release rate. **Figure 14 (a-d)** demonstrates the correlation between MTD and each independent pore parameter.

As shown in **Figure 14 (a)**, MDT decreases as porosity increases. For both pore widths of 0.6 and 2.1 mm, MDT values significantly increase when the pore length is higher than 2 mm, as shown in **Figure 14 (b)**. As pore width decreases, the effect of pore length becomes more considerable and can be used as a design parameter for manipulating drug release rate. Although there is an increase in MDT values of the constructs with pore shapes formed by intersection angles from 90° to 30° (**Figure 14 (c)**), the difference between the lowest and the highest MDT is less than 1%. This can therefore be eliminated as a useful design parameter.

In contrast, the data in **Figure 14 (d)** shows that the staggered structure has a higher MDT than the corresponding lattice structure, and the difference increases with decreasing pore width. These results highlight that as pore width reduces, the effect of staggered filaments becomes more important and can be used as a design parameter. The effects of the pore width on dissolution rate may be explained by the differences in pore void surface area. Larger surface areas result in faster transfer rates into solution. Similarly, pore shape does not affect the surface area expressively hence there is no significant effect on dissolution rates. In the staggered structures, the slowing of dissolution is due to the increase in diffusion path length caused by the obstacle of the alternate extruded filaments (i.e., restricted flow).

Figure 14 (e) shows the relationship between pore width/length ratio of the 3D construct with variable pore geometries and MDT. There is an approximately exponential relationship between pore width/pore length ratio and MDT. The results indicate that MDT is not simply a function of either of the single pore geometries (i.e., porosity, pore length, pore shape and pore alignment), but a function of the combination of both. **Figure 14 (f)** shows a map of pore width on the *X*-axis and pore length on the *Y*-axis and the relationship with MDT. The results show that the pore width has a more dominant effect on the MDT value than the pore length. When pore length was less than three times the pore width, the effect on MDT diminishes; whereas when the pore length is three times higher than the pore width, the MDT increased relatively faster.

These results, for the first time, reveal that the combination of pore width (dependent on the tablet area in the *X*-*Y* plane) and pore length (dependent on the tablet height in the *Z* direction) controls drug release. The pore shape does not have an apparent effect and is, therefore, a less interesting parameter for investigation than other design parameters.

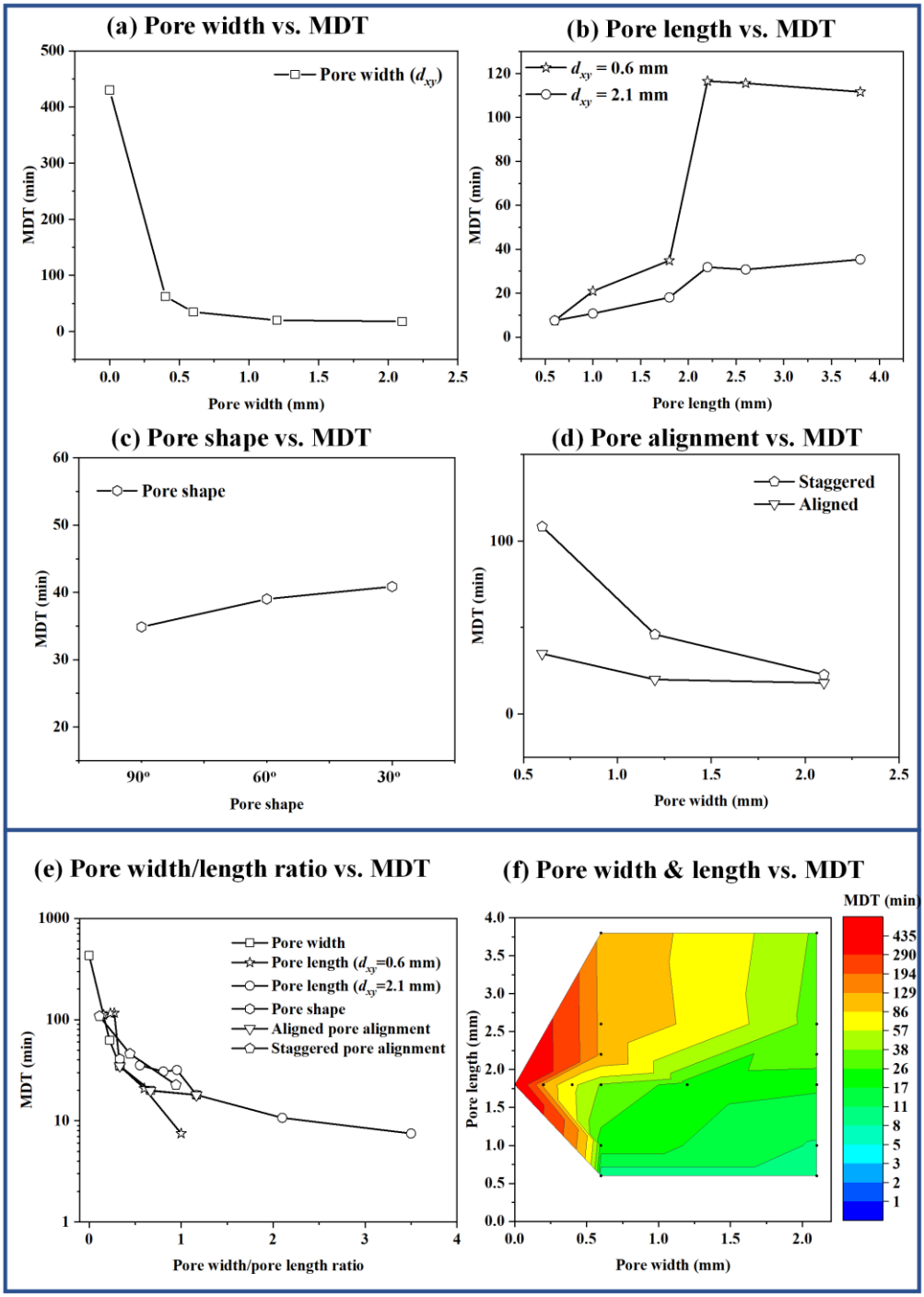

Figure 14. The relationship between (a) porosity and MDT; (b) pore length and MDT; (c) pore shape and MDT; and (d) pore alignment and MDT; (e) pore width/length ratio and MDT; and (f) mapping of pore width, pore length and MDT.

4.2 Mechanisms analysis of drug release from the porous constructs

Since PCL is insoluble in PBS, no swelling or erosion of the ME-AM printed PCL/Ibu 3D construct during the drug release experiment was expected and observed experimentally. The mechanism of drug release, therefore, involved three processes: (1) transfer of drug from the stacked filaments to the interior of the pore; (2) transfer of drug in the pore to the surface of 3D construct and (3) transfer of drug from the surface to the bulk solution. It is worth highlighting that although the total drug content changes with the weight of the 3D printed construct, the drug content per unit weight of the polymer was fixed. Thus, the drug release rate is independent of the 3D printed construct weight.

There are two possible mechanisms involved in drug transfer through the pore: these are diffusion or bulk flow. The hydrodynamics of dissolution baths are complex [40], and it is extremely challenging to identify the hydrodynamic regime the constructs experience during the *in vitro* testing used in this and many other studies in the literature. However, if there is solvent flow through the pores of the 3D constructs, it cannot be that sink conditions can be assumed within all the pores throughout the period of the dissolution test. If this is the case, the rate-determining step for the drug release should be the transfer of the drug from the extruded filaments to the medium in the pore void and the rate of drug release would be independent of the layer number or pore width of the construct. Whilst some contribution of flow cannot entirely be ruled out, the only possible case in which sink conditions occur is in the constructs with 2-layer and 2.1 mm pore width, which has the fastest release profile amongst all the constructs. A working assumption, therefore, is that drug diffusion from the surfaces of the construct into the medium in the pore is a substantial mechanism controlling the drug release.

The constructs of both the 5% and 10% w/w drug loadings show the presence of some crystalline drug at the surfaces of the constructs, as indicted by the PXRD and ATR-FTIR data. Therefore, the total drug dissolution is likely to be a combination of the dissolution of the surface of the drug crystal and diffusion from the polymer matrix. This does not change the fact that the rate of dissolution is dependent on the local concentration of drug in the pore. The continuously increasing drug concentration in

the pore leads to decreases in drug concentration difference of the solution and of the construct. This reduces the driving forces of drug diffusion and the rate of drug release.

In the dissolution bath used, it may be assumed that sink conditions satisfied at the surface layers of the construct in contact with bulk dissolution medium. As shown in **Figure 15**, at the top and bottom surfaces of the pore, the drug diffuses rapidly into bulk medium removing the drug from regions of the pore near to the construct exterior surfaces. This process establishes a concentration gradient along the length of the pore with the lowest concentration at the ends of the pore. Drug depletion from the extruded filaments in this region is rapid causing fastest drug release in comparison to the other interior region of the construct. If the pore length is short enough, diffusion drives the drug to the depletion zone. In this case, the rate of transport depends on the pore length. Increasing pore length increases the diffusion pathlength to the depletion zone, and lengthens the time required for drug to diffuse to the ends of the pore, hence slows down the drug release rate. When the pore length is long enough (critical pore length), the saturation of the drug concentration can be easily reached and maintained. At any pore length longer than the critical pore length, the drug release rate would become independent of the pore length.

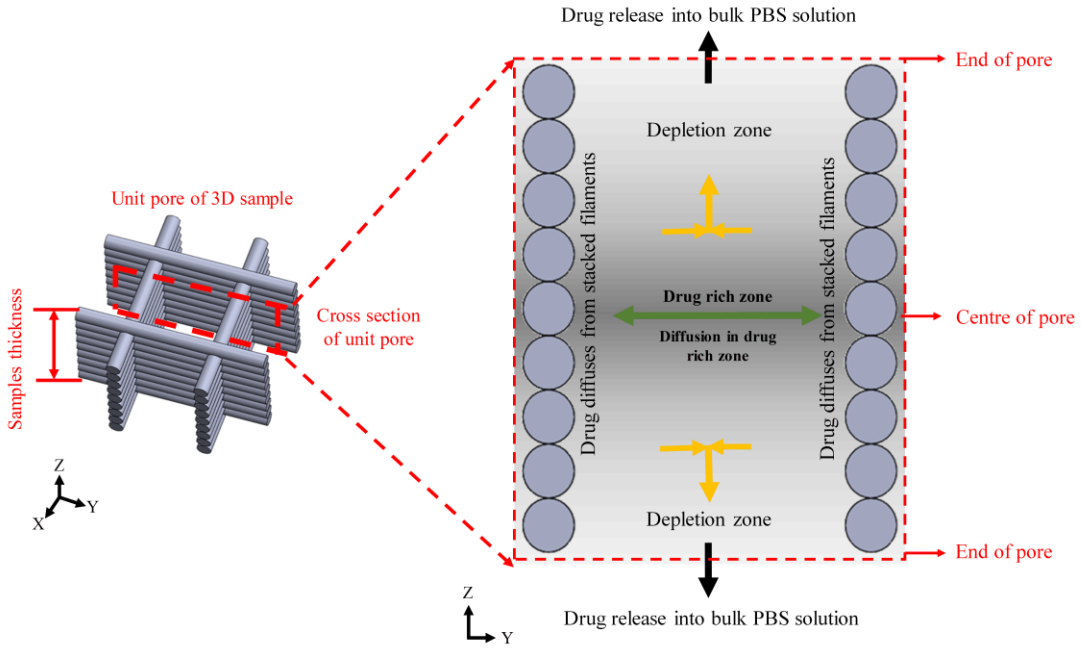

Figure 15. Schematic illustration of the drug diffusion process from the extrusion based additive manufactured PCL/Ibu 3D construct in the bulk PBS buffer.

There should be small variations in behaviour at the end and beginning of the dissolution process as the conditions described above take some time to establish. However, the main parts of the dissolution profile should reflect the same effects of longer pores causing slower drug release. When the pore length is insufficient for the central drug saturation zone to be established and maintained, dissolution rates should be pore length dependent. The results of both 10% and 5% drug loaded constructs show no significant difference in drug release rate at and above 10 layers, indicating that 10-layers provides the critical pore length, and the pore-length independent release can be achieved by designing constructs with more than 10 layers. This result suggests that appropriate geometric design that combined different features within one construct might enable a longer sustained period of consistent drug release compared to typical products.

5 Conclusion

This study systematically investigated the geometrical parameters of 3D printed constructs (i.e., porosity, pore shape, pore length and pore alignment) on drug release behaviour. The SA/V ratios of the ME-AM printed constructs with variable microstructures were predicted using VOLCO model analysis. The results demonstrate that porosity modulates the SA/V ratio, and higher porosities lead to quicker drug release rates. When keeping the SA/V and porosity constant, varying pore shape (lay-down angles change from 90°, 60° and 30°) has no significant effect on altering the drug release rate. For the first time, we report the pore length (or layer number) and pore alignment effects on drug release kinetics. For the materials and the design used in this study, 10-layers was identified as the critical height, and drug release is layer-number dependent if the construct has 10 layers or fewer with pore width of 0.6 and 2.1 mm. However, when increasing the layer number to 10 or more, the drug release rate showed no further change due to the formation of drug depletion zones within long pores. Another noteworthy finding of this study is that staggered structures showed significantly slower drug release rate than aligned lattice structures, and the effects magnified with decreasing pore width. The case study demonstrated that even when porosity and *SA/V* were kept constant, the understanding developed in the study allows pore architecture to be designed to tailor the drug release rate.

This study provided new insights into the influence of geometrical design parameters on drug release kinetics which can be used as new practical design guidance for the controlled performance of ME-AM printed porous materials for a wide range of applications such as agriculture, aquaculture and water treatment as well as personalised pharmaceuticals. Although the effects of the process parameters were not investigated in this study, they could be studied in a dedicated study. For such study, the findings presented here can enable effective evaluation of any indirect effects of process parameters (if they affect the microstructural geometry).

Acknowledgement

This research was funded by the Enabling Innovation: Research to Application (EIRA), a Research England Connecting Capability Fund (CCF) project and the Redistributed Manufacturing in Healthcare Network (RiHN). The RiHN was awarded a grant from the UK Engineering and Physical Sciences Research Council (EPSRC) (Ref. EP/T014970/1).

References

1. Hsiao W-K, Lorber B, Reitsamer H, Khinast J. **3D printing of oral drugs: a new reality or hype?** In: Taylor & Francis; 2018.
2. Vithani K, Goyanes A, Jannin V, Basit AW, Gaisford S, Boyd BJ. **An overview of 3D printing technologies for soft materials and potential opportunities for lipid-based drug delivery systems**. *Pharmaceutical research* 2019; 36(1):1-20.
3. Wening K, Breitkreutz J. **Oral drug delivery in personalized medicine: unmet needs and novel approaches**. *International journal of pharmaceutics* 2011; 404(1-2):1-9.
4. Prasad LK, Smyth H. **3D Printing technologies for drug delivery: a review**. *Drug development and industrial pharmacy* 2016; 42(7):1019-1031.
5. Palo M, Holländer J, Suominen J, Yliruusi J, Sandler N. **3D printed drug delivery devices: perspectives and technical challenges**. *Expert review of medical devices* 2017; 14(9):685-696.
6. Akmal JS, Salmi M, Mäkitie A, Björkstrand R, Partanen J. **Implementation of industrial additive manufacturing: Intelligent implants and drug delivery systems**. *Journal of functional biomaterials* 2018; 9(3):41.
7. Dang HP, Shabab T, Shafiee A, Peiffer QC, Fox K, Tran N, et al. **3D printed dual macro-, microscale porous network as a tissue engineering scaffold with drug delivering function**. *Biofabrication* 2019; 11(3):035014.
8. Martinez PR, Goyanes A, Basit AW, Gaisford S. **Fabrication of drug-loaded hydrogels with stereolithographic 3D printing**. *International journal of pharmaceutics* 2017; 532(1):313-317.
9. Asikainen S, van Bochove B, Seppälä JV. **Drug-releasing biopolymeric structures manufactured via stereolithography**. *Biomedical Physics & Engineering Express* 2019; 5(2):025008.

10. Fina F, Goyanes A, Madla CM, Awad A, Trenfield SJ, Kuek JM, et al. **3D printing of drug-loaded gyroid lattices using selective laser sintering**. *International journal of pharmaceutics* 2018; 547(1-2):44-52.
11. Gieseke M, Senz V, Vehse M, Fiedler S, Irsig R, Hustedt M, et al. **Additive manufacturing of drug delivery systems**. *Biomedical Engineering/Biomedizinische Technik* 2012; 57(SI-1-Track-S):398-401.
12. Wickström H, Hilgert E, Nyman JO, Desai D, Şen Karaman D, De Beer T, et al. **Inkjet printing of drug-loaded mesoporous silica nanoparticles—A platform for drug development**. *Molecules* 2017; 22(11):2020.
13. Boehm RD, Miller PR, Daniels J, Stafslien S, Narayan RJ. **Inkjet printing for pharmaceutical applications**. *Materials Today* 2014; 17(5):247-252.
14. Alhijjaj M, Nasereddin J, Belton P, Qi S. **Impact of processing parameters on the quality of pharmaceutical solid dosage forms produced by fused deposition modeling (FDM)**. *Pharmaceutics* 2019; 11(12):633.
15. Gültekin HE, Tort S, Acartürk F. **An Effective Technology for the Development of Immediate Release Solid Dosage Forms Containing Low-Dose Drug: Fused Deposition Modeling 3D Printing**. *Pharmaceutical research* 2019; 36(9):128.
16. Goyanes A, Martinez PR, Buanz A, Basit AW, Gaisford S. **Effect of geometry on drug release from 3D printed tablets**. *International journal of pharmaceutics* 2015; 494(2):657-663.
17. Korte C, Quodbach J. **3D-printed network structures as controlled-release drug delivery systems: dose adjustment, API release analysis and prediction**. *AAPS PharmSciTech* 2018; 19(8):3333-3342.
18. Zhang B, Huang J, Narayan R. **Gradient scaffolds for osteochondral tissue engineering and regeneration**. *Journal of Materials Chemistry B* 2020.
19. Tan DK, Maniruzzaman M, Nokhodchi A. **Advanced pharmaceutical applications of hot-melt extrusion coupled with fused deposition modelling (FDM) 3D printing for personalised drug delivery**. *Pharmaceutics* 2018; 10(4):203.
20. Zhang B, Chung SH, Barker S, Craig D, Narayan RJ, Huang J. **Direct ink writing of polycaprolactone / polyethylene oxide based 3D constructs**. *Progress in Natural Science: Materials International* 2020.
21. Alhijjaj M, Belton P, Qi S. **An investigation into the use of polymer blends to improve the printability of and regulate drug release from pharmaceutical solid dispersions prepared via fused deposition modeling (FDM) 3D printing**. *European Journal of Pharmaceutics and Biopharmaceutics* 2016; 108:111-125.
22. Kyobula M, Adedeji A, Alexander MR, Saleh E, Wildman R, Ashcroft I, et al. **3D inkjet printing of tablets exploiting bespoke complex geometries for controlled and tuneable drug release**. *Journal of Controlled release* 2017; 261:207-215.
23. Sadia M, Arafat B, Ahmed W, Forbes RT, Alhnan MA. **Channelled tablets: An innovative approach to accelerating drug release from 3D printed tablets**. *Journal of Controlled Release* 2018; 269:355-363.
24. Zhang J, Yang W, Vo AQ, Feng X, Ye X, Kim DW, et al. **Hydroxypropyl methylcellulose-based controlled release dosage by melt extrusion and 3D printing: Structure and drug release correlation**. *Carbohydrate polymers* 2017; 177:49-57.
25. Liang K, Carmone S, Brambilla D, Leroux J-C. **3D printing of a wearable personalized oral delivery device: A first-in-human study**. *Science advances* 2018; 4(5):eaat2544.

26. Pereira GG, Figueiredo S, Fernandes AI, Pinto JF. **Polymer Selection for Hot-Melt Extrusion Coupled to Fused Deposition Modelling in Pharmaceutics**. *Pharmaceutics* 2020; 12(9):795.
27. Melocchi A, Parietti F, Maroni A, Foppoli A, Gazzaniga A, Zema L. **Hot-melt extruded filaments based on pharmaceutical grade polymers for 3D printing by fused deposition modeling**. *International journal of pharmaceutics* 2016; 509(1-2):255-263.
28. Lacroix ACMaD. **The inter-sample structural variability of regular tissue-engineered scaffolds significantly affects the micromechanical local cell environment**. *The royal society publishing* 2015.
29. Gleadall A, Ashcroft I, Segal J. **VOLCO: a predictive model for 3D printed microarchitecture**. *Additive Manufacturing* 2018; 21:605-618.
30. Li J, Lam AT-L, Toh JPW, Reuveny S, Oh SK-W, Birch WR. **Tunable volumetric density and porous structure of spherical poly-ε-caprolactone microcarriers, as applied in human mesenchymal stem cell expansion**. *Langmuir* 2017; 33(12):3068-3079.
31. Yani Y, Kanaujia P, Chow PS, Tan RB. **Effect of API-polymer miscibility and interaction on the stabilization of amorphous solid dispersion: a molecular simulation study**. *Industrial & Engineering Chemistry Research* 2017; 56(44):12698-12707.
32. Zhang B GA, Belton P, Mcdonagh T, Bibb R, and Qi S. **Data for article: New insights into the effects of porosity, pore length, pore shape and pore alignment on drug release from extrusion-based additive manufactured pharmaceuticals, Temporary URL for peer review process: https://figshare.com/s/d98ab20b4b1a2917bded, (2021).**
33. Khan K, KA K. **The concept of dissolution efficiency**. 1975.
34. Kaialy W, Bello H, Asare‐Addo K, Nokhodchi A. **Effect of solvent on retarding the release of diltiazem HC l from Polyox‐based liquisolid tablets**. *Journal of Pharmacy and Pharmacology* 2016; 68(11):1396-1402.
35. Nep EI, Mahdi M, Adebisi A, Dawson C, Walton K, Bills P, et al. **The influence of hydroalcoholic media on the performance of Grewia polysaccharide in sustained release tablets**. *International Journal of Pharmaceutics* 2017; 532(1):352-364.
36. Owusu-Ware SK, Boateng JS, Chowdhry BZ, Antonijevic MD. **Glassy state molecular mobility and its relationship to the physico-mechanical properties of plasticized hydroxypropyl methylcellulose (HPMC) films**. *International journal of pharmaceutics: X* 2019; 1:100033.
37. Abdelrazek E, Hezma A, El-Khodary A, Elzayat A. **Spectroscopic studies and thermal properties of PCL/PMMA biopolymer blend**. *Egyptian Journal of Basic and Applied Sciences* 2016; 3(1):10-15.
38. Kempin W, Franz C, Koster L-C, Schneider F, Bogdahn M, Weitschies W, et al. **Assessment of different polymers and drug loads for fused deposition modeling of drug loaded implants**. *European Journal of Pharmaceutics and Biopharmaceutics* 2017; 115:84-93.
39. Gleadall A, Visscher D, Yang J, Thomas D, Segal J. **Review of additive manufactured tissue engineering scaffolds: relationship between geometry and performance**. *Burns & trauma* 2018; 6(1):19.

40. D'Arcy DM, Corrigan OI, Healy AM. **Evaluation of hydrodynamics in the basket dissolution apparatus using computational fluid dynamics—dissolution rate implications**. *European journal of pharmaceutical sciences* 2006; 27(2-3):259-267.